42nd AIAA Aerospace Sciences Meeting and Exhibit
5 - 8 January 2004, Reno, Nevada

AIAA 2004-254

RECEPTIVITY OF A SUPERSONIC BOUNDARY LAYER OVER A SHARP WEDGE TO WALL BLOWING/SUCTION

Xiaowen Wang * **and Xiaolin Zhong** †
University of California, Los Angeles, California 90095

ABSTRACT

In this paper, we study the receptivity mechanism of a hypersonic boundary layer over a sharp wedge to wall blowing/suction disturbances by using both linear stability theory(LST) and direct numerical simulation(DNS). The work is firstly motivated by Fedorov and Khokhlov's[1] theoretical analysis of the receptivity to wall disturbances of hypersonic boundary layer over a flat plate. The receptivity of a Mach 8.0 flow over a sharp wedge with half-angle 5.3° to periodic blowing/suction disturbances is studied in this paper. The steady base flow is achieved by the combination of TVD and fifth-order shock-fitting method, and its accuracy had been valified in Ma and Zhong's[2] paper. The boundary layer wave mode characteristics of the Mach 8.0 flow over the sharp wedge with half-angle 5.3° is studied by LST. Periodic blowing/suction disturbances are then superimposed to the steady base flow in certain regions on the wedge surface to investigate the receptivity of the boundary layer. Four cases of blowing/suction disturbances are studied in current paper. The results show that the unstable second mode is excited after the synchronization of Mode I and the Mack mode, and the receptivities to blowing/suction disturbances with different frequencies are quite different. The excitation of the unstable second mode is determined by the relation between the blowing/suction region and the synchronization point of the Mack mode and Mode I. The amplitude of the unstable second mode is affected by the profile and region of the blowing/suction disturbance.

INTRODUCTION

The study of laminar-turbulent transition in supersonic and hypersonic boundary layers is very important to the property and safety of supersonic and hypersonic space vehicles. For quiet flow, the semi-empirical e^N method is the most widely used method to predict the transition from laminar flow to turbulent flow. This method assumes that the laminar-turbulent transition occurs in the boundary layer when the most unstable wave mode in the boundary grows up to e^N times as large as its amplitude at the lower branch of the neutral stability curve. The main drawback of the e^N method is that it neglects the effects of environmental disturbances on the boundary layer transition. In the flow with small initial disturbances, the laminar-turbulnet transition procedure can conceptually be divided into three sub-processes: 1) the receptivity process which converts the small initial disturbances into unstable waves in the boundary layer, such as the Tollmien-Schlichting (T-S) waves for incompressible flow and the Mack mode wave for compressible flow. 2) the linear growth process of the boundary layer unstable waves which are the eigen-solutions of the linearized disturbance equations. 3) the nonlinear growth process and breakdown to turbulent. If the initial disturbances in the flow are large enough, the flow can transite to the turbulent state without the appearance of the second sub-process. This is called the bypass transition. The receptivity process is very important because it provides the initial conditions of amplitude, frequency, and phase angle for the unstable waves in the boundary layers[3]. The main objective of a receptivity study is to investigate the properties and mechanisms of initial generation of unstable boundary-layer wave modes by forcing disturbances.

The unstable wave modes in supersonic and hypersonic boundary layers have been studied and identified by Mack[4] using the linear stability theory. Mack found that there are a family of unstable modes in a supersonic boundary layer of relatively high Mach number. Among them, the first mode is the compressible counterpart of T-S waves in incompressible boundary layers, and the second mode becomes the dominant instability in hypersonic boundary layers at Mach numbers larger than 4.0. In this paper, the receptivity of a Mach 8.0 flow over a sharp wedge with half-angle 5.3° to periodic blowing/suction disturbances is studied. Therefore, the receptivities of the second modes to forcing disturbances are the main goal of current study.

The receptivity mechanisms of a Mach 8.0 flow over a sharp wedge to freestream disturbances, i.e., fast and slow acoustic waves, vorticity wave and entrophy wave are extensively studied by Ma and Zhong[2, 5, 6, 7]. They found that there exist a family of stable modes in the supersonic boundary layer in addition to the family of unstable modes. These modes play a very

*Graduate Student Researcher,Mechanical and Aerospace Engineering Department,Student Member AIAA
†Professor, Mechanical and Aerospace Engineering Department,Associate Fellow AIAA.

important role in the receptivity process of the unstable Mack modes, especially the second mode which becomes the dominant instability in flows with Mach numbers larger than 4.0. In this paper, we consider another important type of receptivity associated with wall blowing/suction disturbances. Recently, studies have been carried out about the receptivity of supersonic and hypersonic boundary layers to wall disturbances. EiBler and Bestek[8] studied the receptivities of supersonic boundary layers over the flat plate to wall blowing/suction disturbances with small and moderate amplitudes using direct numerical simulation based on the compressible 3-D Navier-Stokes equations. In their paper, blowing/suction disturbances were introduced into the boundary layer within a narrow disturbance strip on the wall. With finite 2-D disturbances, they found the occurence of fundamental resonance, where the multiple-viscous-solution discribed by Mack[9, 4] is synchronized with the second-mode wave. Fedorov and Khokhlov [1] conducted theoretical analysis of the receptivity of the hypersonic boundary-layer to wall disturbances using asymptotic method and numerical simulation. They investigated the receptivities to different wall disturbances, i.e. vibrations, periodic blowing/suctions, and temperature disturbances, and found that a strong excitation occurred in local regions where forcing disturbances were resonant with boundary layer normal waves. They also found that hypersonic boundary layers were very sensitive to the vertical velocity disturbances which were in resonance with the boundary-layer modes. Unfortunately, the boundary-layer receptivity mechanisms to blowing/suction disturbances are still not so clear, which requires further parametric studies.

GOVERNING EQUATIONS AND NUMERICAL METHODS

The governing equations and the numerical methods are briefly described in this section. In order to simplify the problem, we assume here that the gas is thermally and calorically perfect. In conservative form, the two-dimensional Navier-Stokes equations are written as:

$$\frac{\partial \mathbf{U}^*}{\partial t^*} + \frac{\partial}{\partial x_1^*}(\mathbf{F_{1i}^*} + \mathbf{F_{1v}^*}) + \frac{\partial}{\partial x_2^*}(\mathbf{F_{2i}^*} + \mathbf{F_{2v}^*}) = 0\,, \quad (1)$$

where the superscript "$*$" represents the dimensional variables. $\mathbf{U}^*$ is a vector containing the conservative variables of mass, momentum and energy, and it is expressed as $\{\rho^*, \rho^* u_1^*, \rho^* u_2^*, e^*\}$. $\mathbf{F_{1i}^*}$ and $\mathbf{F_{2i}^*}$ are inviscid flux vectors, i.e. ,

$$\mathbf{F_{1i}^*} = \begin{bmatrix} \rho^* u_1^* \\ \rho^* u_1^{*2} + p^* \\ \rho^* u_1^* u_2^* \\ u_1^*(e^* + p^*) \end{bmatrix}, \quad (2)$$

$$\mathbf{F_{2i}^*} = \begin{bmatrix} \rho^* u_2^* \\ \rho^* u_1^* u_2^* \\ \rho^* u_2^{*2} + p^* \\ u_2^*(e^* + p^*) \end{bmatrix}, \quad (3)$$

$\mathbf{F_{1v}^*}$ and $\mathbf{F_{2v}^*}$ are viscous flux vectors given by

$$\mathbf{F_{1v}^*} = \begin{bmatrix} 0 \\ -\tau_{x_1x_1}^* \\ -\tau_{x_1x_2}^* \\ -\tau_{x_1x_1}^* u_1^* - \tau_{x_1x_2}^* u_2^* - K^* \frac{\partial T^*}{\partial x_1^*} \end{bmatrix}, \quad (4)$$

$$\mathbf{F_{2v}^*} = \begin{bmatrix} 0 \\ -\tau_{x_2x_1}^* \\ -\tau_{x_2x_2}^* \\ -\tau_{x_2x_1}^* u_1^* - \tau_{x_2x_2}^* u_2^* - K^* \frac{\partial T^*}{\partial x_2^*} \end{bmatrix}, \quad (5)$$

with the relations:

$$p^* = \rho^* R^* T^*, \quad (6)$$

$$e^* = \rho^* c_v^* T^* + \frac{\rho^*}{2}(u_1^{*2} + u_2^{*2}), \quad (7)$$

$$\tau_{ij}^* = \mu^*(\frac{\partial u_i^*}{\partial x_j^*} + \frac{\partial u_j^*}{\partial x_i^*}) - \frac{2}{3}\mu^* \frac{\partial u_k^*}{\partial x_k^*}\delta_{ij}, \quad (8)$$

for i, j=1, 2. In the numerical simulations, the viscosity coefficients μ^* and heat conductivity coefficients K^* are calculated using Sutherland's law together with a constant Prandtl number, Pr.

$$\mu^*(T^*) = \mu_r^* \left(\frac{T^*}{T_r^*}\right)^{3/2} \frac{T_r^* + T_s^*}{T^* + T_s^*}, \quad (9)$$

$$K^*(T^*) = \frac{\mu^*(T^*) c_p}{Pr}, \quad (10)$$

where $\mu_r^* = 1.7894 \times 10^{-5} N - Sec/m^2$,$T_r^* = 288.0K$, $T_s^* = 110.33K$. In this paper, all the dimensional flow variables are nondimensionalized by the corresponding freestream parameters.

A fifth-order shock-fitting method of Zhong[10] is used to solve the two-dimensional Navier-Stokes equations in the flow field bounded by the oblique shock and the wedge surface. The shock-fitting method treats the oblique shock as a moving boundary. The flow variables behind the shock are determined by Rankine-Hugoniot relations across the shock and a characteristic compatibility relation from behind the shock. The transient movement of the shock and its interaction with the disturbances originated from blowing/suction regions on the wedge surface are solved as a part of the solutions. The use of shock-fitting method make it possible to use high-order finite difference scheme for spatial discretization. Fifth-order upwind scheme and sixth-order central

scheme are applied for the spatial discretizations of convective terms and viscous terms respectively. The spatial discretizations of the governing equations lead to a system of first-order ordinary differential equations. Explicit Runge-Kutta method is then used for temporal discretization.

The problem still left is that the fifth-order shock-fitting method can not solve the Navier-Stokes equations accurately within the leading edge region of the sharp wedge because of the singularity at the leading point. This problem is overcomed by introducing a second-order TVD code developed by Zhong and Lee[11]. The steady base flow within the leading edge region of the sharp wedge with half-angle 5.3° is solved by using the TVD code with very fine grids, and it is then used as the inflow conditions to start the solution procedure by the fifth-order shock-fitting method.

FLOW CONDITIONS AND BLOWING/SUCTION DISTURBANCES

The receptivity of a Mach 8.0 boundary-layer flow over a sharp wedge with half-angle 5.3° has been studied recently [12, 7]. And the receptivity mechanisms of the boundary-layer to freestream disturbances, i.e. fast and slow acoustic waves, vorticity waves and entropy waves, have been investigated extensively. But the boundary-layer receptivity mechanisms to blowing/suction disturbances have not been studied, which requires further parametric studies. The flow conditions in this paper are the same as those in Ma and Zhong's paper [7] on the receptivity of a Mach 8.0 flow over a sharp wedge to freestream disturbances, i.e. ,

$$M_\infty = 8.0\,, \qquad T^*_\infty = 54.78\,K\,,$$
$$p^*_\infty = 389Pa\,, \qquad Pr = 0.72\,,$$
$$Re^*_\infty = \rho^*_\infty U^*_\infty/\mu^*_\infty = 8.2\times 10^6/m\,.$$

In many figures of this paper, the results are plotted as a function of dimensional coordinate s^* along the wedge surface which is the dimensional coordinate in meter measured along the wedge surface from the leading edge. For the current simulations, the dimensional s^* coordinate in the figures can be easily converted to nondimensional local Reynolds number according to the following formula:

$$Re_s = Re^*_\infty\ s^* = 8.2\times 10^6 s^*\,, \tag{11}$$

Because the steady flow and geometry are symmetric, only the upper half part of the flow field is considered in this paper. The computational domain of the simulations using the fifth-order shock-fitting method begins at $s^* = 0.00409m$ and ends at $s^* = 1.33784m$, corresponding to the local Reynolds number Re_s ranging from 3.3538×10^4 to 1.097×10^7. In the studies of boundary-layer stability, the following Reynolds number, R, based on the local length scale of boundary-layer thickness are often used:

$$R = \frac{\rho^*_\infty u^*_\infty L^*}{\mu^*_\infty}\,, \tag{12}$$

where the local length scale of boundary-layer thickness L^* is defined as

$$L^* = \sqrt{\frac{\mu^*_\infty s^*}{\rho^*_\infty u^*_\infty}}\,. \tag{13}$$

Hence, the relation between R and local Reynolds number Re_s is

$$R = \sqrt{Re_s}\,. \tag{14}$$

In terms of R, the full computational domain of the current simulations spans from $R = 183.1$ to $R = 3312.1$. In the actual simulations, the computational domain is divided into 27 sub-zones with a total of 5336 grid points in the streamwise direction. 121 grid points are used in the normal direction. And 41 points are used in the overlap regions between two neighboring zones which are sufficient to make the solution accurate and smooth for the whole region. Grid stretching function is used in normal direction to cluster more points inside the boundary layer near the wall. While the grid points are distributed uniformly in the streamwise direction. The numerical accuracy of the results based on this grid structure has been evaluated by grid refinement studies to ensure grid independence of the numerical solutions.

After the steady base flow is achieved, the blowing/suction disturbances with multiple frequecies are then superimposed at certain region on the wedge surface. With the shock-fitting method, the effects of the interactions between the oblique shock and blow/suction disturbances are accurately taken into account. We assume that blowing/suction disturbances only relate to the perturbations of normal velocity, and no disturbances of streamwise velocity, pressure and temperature are superimposed on the wall. So the disturbances of nondimensional flow variables in the blowing/suction regions on the wedge surface can be written in the following form:

$$\begin{Bmatrix} u' \\ v' \\ p' \\ T' \end{Bmatrix} = \begin{Bmatrix} 0 \\ \sum \epsilon_n \beta(s^*) Sin(\omega^*_n t^*) \\ 0 \\ 0 \end{Bmatrix}\,, \tag{15}$$

where ϵ_n is a small nondimensional parameter representing the amplitude of normal velocity disturbance with frequency f^*_n. The amplitudes of blowing/suction disturbances are carefully chosen so that the nondimensional amplitudes of the perturbations are at least one order of magnitude larger than the nondimensional amplitude of the maximum numerical noise, while they are small enough to preserve the linearity of boundary layer wave modes. To make the results of different

frequencies comparable, we choose the same amplitude for all the disturbances. $\beta(s^*)$ is a function defined on the blowing/suction region which represents the profile of the normal velocity disturbances. With different $\beta(s^*)$ functions, we can superimpose different kinds of blow/suction disturbances. As before, s^* is the coordinate along the wedge surface. ω_n^* is the circle frequency of normal velocity disturbance with frequency f_n^*.

$$\omega_n^* = 2\pi f_n^* \,, \tag{16}$$

$$f_n^* = 1.492 \times 10^4 n(Hz) \,, \tag{17}$$

The frequency is characterized by a nondimensional frequency F defined by

$$F = \frac{\omega^* \mu_\infty^*}{\rho_\infty^* u_\infty^{*2}} \,, \tag{18}$$

The nondimensional circular frequency is then defined as

$$\omega = RF \,, \tag{19}$$

STEADY BASE FLOW SOLUTIONS

The steady base flow is calculated by a fifth-order shock-fitting method, which takes into account the effects of oblique shock, shock/boundary-layer interaction and flow compressibility. For the first zone, the inflow conditions are obtained from the results of TVD method, which had been validated in cases of supersonic and hypersonic steady flows over flate plates in Ma and Zhong's paper[6]. Figure 1 compares the steady density contours obtained from the TVD method with those from the fifth-order shock-fitting method. We find that there is excellent agreement between the contours within the overlap region. This implies that it is accurate enough to use TVD solutions as inflow conditions for the high-order shock-fitting calculation.

Figure 2 shows the pressure contours of the steady base flow calculated by fifth-order shock-fitting method. The upper boundary of the flow field represents the oblique shock. Compared with the case of the Mach 4.5 flow over a flat plate[6],the oblique shock is pushed closer to the wall surface because of the higher Mach number. In the flow field, pressure is almost constant across the boundary layer and along the Mach lines, which is consistent with the boundary-layer theory and supersonic aerodynamics. Figure 3 compares the distribution of pressure along the wedge surface with that of the theoretical inviscid solution. Near the leading edge, the strong interaction between inviscid external flow and viscous boundary-layer results in the great pressure gradient. With this kind of interaction becoming weaker and weaker downstream, the pressure becomes a constant, but its value still greater than that of the theoretical inviscid oblique shock solution. This is the contribution of viscous effects.

The shock front postion and the distribution of shock angle along the wedge surface are shown in Figure 4. This figure tells that the shock front is not a straight line with the shock angle decreasing from 14.793° near the leading edge to 11.314° at the exit of the computational dormain. Figure 5 gives the distribution of the Mach number behind the shock. It shows that Mach number increases from 5.911 near leading edge to 6.743 at the exit of the computational dormain. For inviscid hypersonic flow over a wedge with half angle 5.3°, the theoretical shock angle is 11.102°, and the theoretical Mach number behind the shock is 6.798. So the results of shock angle and Mach number behind the oblique shock from the simulation appproach the inviscid theoretical solutions in the region downstream where shock moves far away from the boundary layer and the interaction between inviscid external flow and the viscous boundary layer becomes negligible.

BOUNDARY-LAYER WAVE MODES CHARACTERISTICS

After the steady base flow is achieved, the characteristics of boundary-layer normal wave modes of the Mach 8.0 flow over the sharp wedge is studied by the linear stability theory. However the numerical solutions are inconvenient for LST analysis, because the flow field information must be totally changed if we change the LST analysis to a different location. In this paper, the self-similar boundary-layer solutions are used instead to investigate the characteristics of the boundary-layer wave modes. Figure 6 compares the streamwise velocity and it first-order derivative between the numerical solution and the self-similar solution. Figure 7 compares the second-order derivative of streamwise velocity between the numerical solution and the self-similar solution. And Figure 8 compares the temperature and it first-order derivative between the numerical solution and the self-similar solution. For all comparisons, there is little difference between the self-similar boundary-layer solution and the steady base flow solved by numerical simulations. Our calculations have proved that the linear stability characteristics based on self-similar boundary-layer solution are very close to those based on numerical solutions, although shock/boundary-layer interaction and flow compressibility effects are neglected in the self-simliar boundary-layer solution.

The grobal and local multi-domain spectral methods proposed by Malik[13] are employed in this paper to solve the linear stability equations. The global method is used to solve all approximate eigenvalues. While the local method is a shooting method which is capable of shooting the more accurate eigenvalue of a specific mode. The combination of the global and local methods makes it possible to get the accurate eigenvalues. The engenvalue α, nondimensionalized by the local boundary layer thickness, is usually a complex number, and

it can be expressed as

$$\alpha = \alpha_r + i\alpha_i \,, \tag{20}$$

where $-\alpha_i$ is the local growth rate, α_r is the local wave number which can be used to define the non-dimensional local phase velocity:

$$a = \frac{\omega}{\alpha_r} \,, \tag{21}$$

Both the wave number and the phase velocity can be used to characterize the normal modes inside the boundary layer.

When one accurate eigenvalue is got, we can track this eigenvalue to get the spectra of the normal mode. The whole procedure to track a specific mode can be divided into three steps: 1) getting all eigenvalues by global method and identifying the eigenvalue of the specific mode by investigating the corresponding eigenvector, 2) taking the approximate eigenvalue got from global method as the initial guess value and shooting the more accurate eigenvalue of the specific mode using local method, 3) tracking the mode. The final step can be different with different problems. If we want to track the spectra of one mode with fixed frequency, we can use the accurate eigenvalue as the initial guess value to shoot the eigenvalue for neighboring locations by changing the location upstream or downstream slowly. If we want to track the spectra of one mode at the fixed location, we can use the accurate eigenvalue as the initial guess value to shoot the eigenvalue for the disturbance with neighboring frequency by increasing or decreasing the frequency little by little. And if we want to track the neutral curve of one mode, we use the neutral point as the initial guess value to shoot the neighboring neutral point by changing the location and the frequency slowly and simultaneously.

For current LST analysis, the adiabatic temperature condition is used on the wedge surface. Figure 9 shows all the eigenvalues of boundary layer normal modes for the disturbance with the nondimensional frequency $F = 5.778 \times 10^5$ at the location $R = 1980.44$ ($s^* = 0.48036m$). Dispite the continuous modes, there are two discrete modes marked by circles. Investigations of the corresponding eigenvectors prove that one is the second mode (Mack mode), the orther is a stable mode called Mode I in Ma and Zhong's papers[2, 5]. It also shows that Mode I starts from continuous modes on the left side of the Figure and passes continuous modes in the middle with increasing ω. Figure 10 compares the spectra of the non-dimensional phase velocities of normal modes inside the boundary layer with different frequencies. It shows that the spectra of phase velocities are almost frequency independent. From upstream to downstream, the Mack mode synchronizes with Mode I at $\omega = 0.11443, a/u_\infty = 0.93349$ because the non-dimensional phase velocities of Mode I and the Mack mode are the same at this point, and their eigenfunctions have very similar profiles as shown in Figure 11. Before the synchronization with Mode I, the Mack mode is called the first mode. When it synchronizes with Mode I, the first mode changes to the second mode. At further downstream, there exist Mode II, Mode III, Mode IV, etc, and the Mack mode will synchronize with these modes consequently and change itself after the synchronizations. The synchronization point of Mode I and Mack mode is quite important, because the unstable second mode is excited after the synchronization at this point. Comparison of the nondimensional wave numbers and growth rates with different frequencies are given in Figure 12 and Figure 13. The non-dimensional wave numbers are almost the same, and the growth rates with different frequencies are similar. It also shows that the second mode is the most unstable mode, Mode I and Mode II are both stable. The neutral curve of Mack mode for the Mach 8.0 flow over the sharp wedge with half angle 5.3° had got in Ma and Zhong's[7] paper. Figure 14 shows the neutral curve of the Mack mode for the Mach 8.0 flow over the sharp wedge. It shows that the critical local Reynolds number R for boundary-layer instability is 210. In order to show the properties of the second-mode Branch II neutral points at different frequencies, the neutral curve of Mack mode is redrawn in terms of ω via R in Figure 15. When R increases from 1000 to 2287 (s^* from $0.12247m$ to $0.63784m$), the second mode Branch II neutral point in terms of ω increases from 0.158 to 0.167. By extrapolation, this result can be used to predict the location of the second-mode Branch II neutral point for R > 1000.

RECEPTIVITY TO BLOWING/SUCTION DISTURBANCES

In this paper, multi-frequency blowing/suction disturbances are introduced to the steady base flow by superimposing normal velocity oscillations at certain region on the wedge surface. The receptivities of the hypersonic boundary layer to multi-frequency blowing/suction disturbacnes are investigated by the direct numerical simulation. After the blowing/suction disturbances are superimposed on the wedge surface, the fifth-order shock-fitting method is used to simulate the unsteady flow until the flow field reaches a periodic state. The computational dormain of unsteady flow are the same as that of steady base flow simulations, but the isothermal temperature condition is applied on the wedge surface. This is a physical assumption to unsteady flow simulation, because the frequencies of blowing/suction disturbances are usually so high that the temperature on the wedge surface is almost unchanged during the disturbance period.

Four cases of blowing/suction disturbances are investigated in this paper:

case 1: blowing/suction disturbances with ten fre-

quencies (F_n with n from 6 to 15) are introduced in the region on the wedge surface from $s_i^* = 0.20184m$ to $s_e^* = 0.21384m$ (corresponding to R from 1283.75 to 1321.36). The sine-like profile function of the blowing/suction disturbances is $\beta_n(l) = 20.25l^5 - 35.4375l^4 + 15.1875l^2$ if $l <= 0.5$ and $\beta_n(l) = -\beta_n(1.0-l)$ if $l >= 0.5$, where l is a non-dimensional coordinate defined within the blowing/suction region: $l = (s^* - s_i^*)/(s_e^* - s_i^*)$.

case 2: blowing/suction disturbances with ten frequencies (F_n with n from 6 to 15) are introduced in the region on the wedge surface from $s^* = 0.20184m$ to $s^* = 0.21384m$(corresponding to R from 1283.75 to 1321.36). The rectangular-like profile function of the blowing/suction disturbances is $\beta_n(s^*) = 1.0$.

case 3: blowing/suction disturbances with fifteen frequencies (F_n with n from 1 to 15) are introduced in regions on the wedge surface centered at $s^* = 0.4m$. The length scale of the blowing/suction region for disturbance with frequency F_n is equal to the disturbance wavelength. So for disturbances with different frequencies, the scales of blowing/suction regions are different. And they can be calculated by the equation:

$$\lambda_n^* = \frac{au_\infty}{f_n^*}\,, \tag{22}$$

where a is the non-dimensional local phase velocity. The sine-like profile function of the blowing/suction disturbances is defined simliar to case 1.

case 4: blowing/suction disturbances with fifteen frequencies (F_n with n from 1 to 15) are introduced in regions on the wedge surface centered at $s^* = 0.4m$. The length scales of the blowing/suction regions for the multi-frequency disturbances are the same as those in case 3. And The rectangular-like profile function of the blowing/suction disturbances is the same as case 2.

The frequency, non-dimensional frequency and wavelength of multi-frequency blowing/suction disturbances are listed in Table 1.

Table 1: The frequency, non-dimensional frequency and wavelength of multi-frequency blowing/suction disturbances

n	$f_n^*(kHz)$	$F_n \times 10^6$	$\lambda_n^* \times 10^2$
1	14.92	9.63	7.39352
2	29.84	19.26	3.669676
3	44.76	28.89	2.46451
4	59.68	38.52	1.84838
5	74,60	48.15	1.47870
6	89,52	57.78	1.23225
7	104.44	67.41	1.05622
8	119.36	77.04	0.92419
9	134.28	86.67	0.82150
10	149.20	96.30	0.73935
11	164.12	105.93	0.67214
12	179.04	115.56	0.61613
13	193.96	125.19	0.56873
14	208.88	134.82	0.52811
15	223.80	144.45	0.49290

Result discussion for case 1

Figure 16 shows the distribution of instantaneous pressure disturbance along the wedge surface. In the disturbance field, there are multiple peaks of amplitude. The modulations of the muliple frequencies result in the oscillations of the instantaneous pressure disturbance. The amplification of the amplitude peak indicates the generation of unstable mode. In order to investigate the effect of frequency, fast Fourier transformation (FFT) is applied to the instantaneous disturbance field. Figure 17 and Figure 18 compare the amplitudes of pressure perturbations along the wedge surface with different frequecies. The initial amplitudes of blowing/suction disturbances are the same for different frequencies. The perturbations with frequencies F_6,F_7,F_8 and F_9 grow up after the blowing/suction region then decrease further downstream. This indicates that unstable modes with corresponding frequencies are excited by these blowing/suction disurbances. While the perturbations with other frequencies decrease monotonically because they can not excite the unstable mode.

To inverstigate the properties of the unstable mode, Fourier transformation is applied to the real perturbation, which leads to:

$$p^{*\prime}(x,y,t) = \sum_{n=1}^{N} |p^{*\prime}{}_n(x,y)| e^{i\,[\phi_n'(x,y) - \omega_n^* t^*]}\,, \tag{23}$$

where ω_n^* is circle frequency of the perturbation with the frequency F_n, $p^{*\prime}(x,y,t)$ represents the instantaneous pressure disturbance, $|p^{*\prime}{}_n(x,y)|$ and $\phi_n'(x,y)$ are real variables representing the perturbation amplitude and phase angle. These variables indicate a local wave number α_{rn} and a local growth rate α_{in} of the perturbation with the frequency F_n, which can be calculated by,

$$\alpha_{rn} = \frac{d\phi_n'}{ds^*}, \tag{24}$$

$$\alpha_{in} = -\frac{1}{|p^{*\prime}{}_n|}\,\frac{d|p^{*\prime}{}_n|}{ds^*}\,, \tag{25}$$

The wave number, growth rate and non-dimensional phase velocity of the unstable mode are inverstigated for the blowing/suction disturbances with frequencies F_6 and F_7.

Figure 19 compares the wave number α_r solved by DNS and that of the unstable second mode got by LST with the frequency F_6. Figure 20 compares the growth rate α_i solved by DNS and that of the unstable second mode got by LST with the frequency F_6. And Figure 21 compares the non-dimensional phase velocity a/u_∞ solved by DNS and that of the unstable second mode

got by LST with the frequency F_6. The agreements in these figures indicate that the unstable mode is the second mode. Figure 22 compares the the eigenfunction of the second mode and the instantaneous pressure perturbation(frequency F_6) from DNS at the position $s^* = 0.47784m$ ($R = 1975.23$). In this case, the non-dimensional displacement thickness of the boundary layer is 16.45. Within the boundary layer, the pressure perturbation with frequency F_6 fits well with the eigenfunction of second mode, indicating also that the unstable mode is the second mode.

Figure 23 compares the wave number α_r solved by DNS and that of the unstable second mode got by LST with the frequency F_7. Figure 24 compares the growth rate α_i solved by DNS and that of the unstable second mode got by LST with the frequency F_7. And Figure 25 compares the non-dimensional phase velocity a/u_∞ solved by DNS and that of the unstable second mode got by LST with the frequency F_7. The agreements in these figures indicate that the unstable mode is the second mode. Figure 26 compares the the eigenfunction of the second mode with the instantaneous pressure perturbation(frequency F_7) from DNS at the position $s^* = 0.37784m$ ($R = 1756.43$). In this case, the non-dimensional displacement thickness of the boundary layer is 16.45. Within the boundary layer, the pressure perturbation with frequency F_7 fits well with the eigenfunction of second mode, indicating also that the unstable mode is the second mode.

Figure 10 shows that the Mack mode and Mode I synchronizes at the point $\omega_s = 0.11443, a_s = 0.93349$. After the synchronization, the stable Mode I excites the unstable second mode. The unstable properties of the second mode make the perturbations growing up. In s^* coordinates, the positions of the synchronization point are different for the blowing/suction disturbances with different frequencies. They can be calculated using

$$s^*_{sn} = \frac{(\omega_s/F_n)^2}{Re_\infty}\,, \tag{26}$$

Figure 13 shows that the position of Branch II neutral point of second mode is at $\omega_{II} = 0.22755, \alpha_{iII} = 0.0$. And the coordinates ω_{II} is independent of the frequencies of blowing/suction disturbances. After this point, the second mode becomes stable. In s^* coordinates, the positions of the Branch II neutral point are different for the blowing/suction disturbances with different frequencies. They can be calculated using

$$s^*_{IIn} = \frac{(\omega_{II}/F_n)^2}{Re_\infty}\,, \tag{27}$$

Table 2 provides non-dimensional frequency, s^* coordinates of the synchronization points and the Branch II neutral points for the multi-frequency disturbances.

Compared Figure 17 and Figure 18 with table 2, we notice that the perturbations with frequencies F_n (n from 6 to 9) start to grow up at the positions very close to the s^*_{sn} in table 2. This means that the second mode is excited by the synchronization of Mode I and the Mack mode. But the perturbations with frequencies F_n (n from 6 to 9) decrease far before the s^*_{IIn} in table 2. This means that the LST result can not predict the Branch II neutral points accurately. The amplitude peaks are quiet different, and it seems here that the amplitude peak increases with the distance between the synchronization point and the blowing/suction region increasing. For the perturbations with frequencies F_n (n> 9), the synchronization points of Mode I and the Mack mode are at the upstream of blowing/suction regions. So no synchronizations between Mode I and the Mack mode happen, and no second modes are excited.

Table 2: Non-dimensional frequency, s^* coordinates of the synchronization point and the Branch II neutral point for multi-frequency disturbances

n	$F_n \times 10^6$	s^*_{sn} (m)	s^*_{IIn} (m)
1	9.63	16.9885	68.38297
2	19.26	4.2471	17.09574
3	28.89	1.8876	7.59811
4	38.52	1.0618	4.27394
5	48.15	0.6795	2.73532
6	57.78	0.4719	1.89953
7	67.41	0.3467	1.39557
8	77.04	0.2653	1.06848
9	86.67	0.2097	0.84423
10	96.30	0.1699	0.68383
11	105.93	0.1404	0.56515
12	115.56	0.1180	0.47488
13	125.19	0.1005	0.40463
14	134.82	0.0867	0.34889
15	144.45	0.0493	0.30392

Result discussion for case 2

Figure 27 gives the distribution of instantaneous pressure disturbance along the wedge surface. In the disturbance field, there is the same number of amplitude peaks as that in Figure 16 although the profile of blowing/suction disturbances is changed. This means that the characteristics of pressure disturbance distribution are the result of frequency modulations. The amplitude peak increases at first and then decreases. This means that the unstable second mode is excited at first and it becomes stable later. In order to investigate the effect of frequency, fast Fourier transformation (FFT) is also applied to the instantaneous disturbance field. Figure 28 and Figure 29 compare the amplitudes of pressure perturbations along the wedge surface with different frequecies. The initial amplitude of blowing/suction disturbances are the same for different frequencies and

the same as in case 1. The perturbations with frequencies F_6,F_7,F_8 and F_9 grow up after the blowing/suction region then decrease downstream. This indicates that second modes with corresponding frequencies are excited by these blowing/suction disurbances. The amplitude peaks are also quiet different, but the amplitude peak does not increase with the distance between the synchronization point and the blowing/suction region increasing as in case 1.While the perturbations with other frequencies decrease monotonically because they can not excite the unstable second mode.

Compared Figure 28 and Figure 29 with table 2, we find that the perturbations with frequencies F_n (n from 6 to 9) start to grow up at the positions very close to the s^*_{sn} in table 2. This indicates that the second mode is excited by the synchronization of Mode I and the Mack mode. But the perturbations with frequencies F_n (n from 6 to 9) decrease far before the s^*_{IIn} in table 2. This indicates that the LST result can not predict the Branch II neutral points accurately. For the perturbations with frequencies F_n (n$>$ 9), the synchronization points of Mode I and the Mack mode are at the upstream of blowing/suction regions. So no synchronizations between Mode I and the Mack mode happen, and no second modes are excited.

Compared Figure 28 and Figure 29 with Figure 17 and Figure 18, we find that the amplitude peaks of pressure perturbations for blowing/suction disturbances case 2 are much weaker than those for blowing/suction disturbances case 1. This means that the amplitude peaks of pressure perturbations are sensitive to the different profiles of blowing/suction disturbances.

Result discussion for case 3

Figure 30 gives the distribution of instantaneous pressure disturbance along the wedge surface. In the disturbance field, there are multiple peaks of amplitude. The modulations of the muliple frequencies result in the oscillations of the instantaneous pressure disturbance. The amplification of the amplitude peak indicates the generation of unstable second mode. In order to investigate the effect of frequency, fast Fourier transformation (FFT) is applied to the instantaneous disturbance field. Figure 31, Figure 32 and Figure 33 compare the amplitudes of pressure perturbations along the wedge surface with different frequecies. The initial amplitudes of blowing/suction disturbances are the same for different frequencies. The perturbations with frequencies F_4, F_5, and F_6 grow up after the blowing/suction region. This indicates that second modes with corresponding frequencies are excited by these blowing/suction disurbances. The amplitude peaks are quiet different for different frequencies, but the amplitude peak does not increase with the distance between the synchronization point and the blowing/suction region increasing as in case 1. The perturbations with frequencies F_1, F_2, and F_3 oscillate after the blowing/suction region and grow up very slowly. While the perturbations with other frequencies decrease monotonically because they can not excite the unstable second mode.

Compared Figure 31, Figure 32 and Figure 33 with table 2, we notice that the perturbations with frequencies F_n (n from 4 to 6) start to grow up at the positions very close to the s^*_{sn} in table 2. This indicates that the second mode is excited by the synchronization of Mode I and the Mack mode. But the perturbation with frqeuency F_6 decreases far before the s^*_{IIn} in table 2. This indicates that the LST result can not predict the Branch II neutral points accurately. The perturbations with frequencies F_n (n from 1 to 3) start to grow up very slowly at the positions far upstream to the s^*_{sn} in table 2. This indicates that the oscillations don't result from the second mode. They maybe come from the frequency modulations. For the perturbations with frequencies F_n (n$>$ 6), the synchronization points of Mode I and the Mack mode are at the upstream of blowing/suction regions. So no synchronizations between Mode I and the Mack mode happen, and no second modes are excited.

Result discussion for case 4

Figure 34 gives the distribution of instantaneous pressure disturbance along the wedge surface. In the disturbance field, there is the same number of amplitude peaks as that in Figure 30 although the profile of blowing/suction disturbances is changed. This means that the characteristics of pressure disturbance distribution are the result of frequency modulations. The amplification of the amplitude peak indicates the generation of unstable second mode. In order to investigate the effect of frequency, fast Fourier transformation (FFT) is applied to the instantaneous disturbance field. Figure 35, Figure 36 and Figure 37 compare the amplitudes of pressure perturbations along the wedge surface with different frequecies. The initial amplitudes of blowing/suction disturbances are the same for different frequencies and the same as in case 3. The perturbations with frequencies F_4, F_5, and F_6 grow up after the blowing/suction region. This indicates that second modes with corresponding frequencies are excited by these blowing/suction disurbances. The amplitude peaks are quiet different for different frequencies, but the amplitude peak does not increase with the distance between the synchronization point and the blowing/suction region increasing as in case 1. The perturbations with frequencies F_1, F_2, and F_3 oscillate after the blowing/suction region and grow up very slowly. While the perturbations with other frequencies decrease monotonically because they can not excite the unstable second mode.

Compared Figure 35, Figure 36 and Figure 37 with table 2, we find that the perturbations with frequencies

F_n (n from 4 to 6) start to grow up at the positions very close to the s^*_{sn} in table 2. This indicates that the second mode is excited by the synchronization of Mode I and the Mack mode. But the perturbation with frequency F_6 decreases far before the s^*_{IIn} in table 2. This indicates that the LST result can not predict the Branch II neutral points accurately. The perturbations with frequencies F_n (n from 1 to 3) start to grow up very slowly at the positions far upstream to the s^*_{sn} in table 2. This indicates that the oscillations don't result from the second mode. They maybe come from the frequency modulations. For the perturbations with frequencies F_n (n$>$ 6), the synchronization points of Mode I and the Mack mode are at the upstream of blowing/suction regions. So no synchronizations between Mode I and the Mack mode happen, and no second modes are excited.

Compared Figure 35, and Figure 36 and Figure 37 with Figure 31, Figure 32 and Figure 33, we find that the amplitude peaks of pressure perturbations for blowing/suction disturbances case 4 are much weaker than those for blowing/suction disturbances case 3. This means that the amplitude peaks of pressure perturbations are sensitive to the different profiles of blowing/suction disturbances.

CONCLUSION

The receptivity of a hypersonic boundary layer to periodic blowing/suction disturbances for a two dimensional Mach 8.0 flow over a sharp wedge with half angle 5.3° has been studied by both linear stability theory and direct numerical simulation. The main objective of the study on the receptivity of the hypersonic boundary-layer flow is to investigate the generation and growth of boundary-layer normal modes, especially the unstable second Mack mode excited by blowing/suction disturbances. The steady base flow is achieved, and the characteristics of normal boundary wave modes are analysized using LST. Blowing/suction disturbances are introduced by superimposing the normal velocity disturbances with different frequencies in certain regions on the wedge surface. Four different cases of multi-frequency blowing/suction disturbances are superimposed to the steady base flow to investigate the receptivity mechanism .

All the results show that receptivities to blowing/suction disturbances with different frequencies are quite different. The unstable second mode is excited by the synchronization of Mode I and the Mack mode. The positions of the synchronization point are quite different for the blowing/suction disturbances with different frequencies. The excitation of the unstable second mode is determined by the relation between the blowing/suction region and the synchronization point of the Mack mode and Mode I. If the blowing/suction region is upstream to the synchronization point, unstable second mode is excited. Otherwise, no second mode is excited.

The postions where the second modes are excited by blowing/suction disturbances with different frequencies can be accurately predicted by LST. While the second mode becomes stable much earlier than the positions of the Branch II neutral point predicted by LST, this means that LST can not predict the Branch II neutral point second mode accurately.

The amplitude peaks of the pressure perturbations are affected by the regions and profiles of blowing/suction disturbances. Further studies are needed to investigate the growth of the unstable second mode and the oscillations of the pressure perturbations with lower frequencies in the blowing/suction disturbances case 3 and case 4.

ACKNOWLEDGMENTS

This work was sponsored by the Air Force Office of Scientific Research, USAF, under AFOSR Grant #F49620-00-1-0101, monitored by Dr. John Schmisseur. The views and conclusions contained herein are those of the author and should not be interpreted as necessarily representing the official policies or endorsements, either expressed or implied, of the Air Force Office of Scientific Research or the U.S. Government.

References

[1] A. V. Fedorov and A. P. Khokhlov. Receptivity of Hypersonic Boundary Layer to Wall Disturbances. *Theoretical and Computational Fluid Dynamics*, 15:231–254, 2002.

[2] Y.Ma and X.Zhong. Receptivity of a supersonic boundary layer over a flat plate. Part 1:Wave Structures and Interactions. *Journal of Fluid Mechanics*, vol.488, pp.31-78, 2003.

[3] M. E. Goldstein and L. S. Hultgren. Boundary-Layer Receptivity to Long-Wave Free-Stream Disturbances. *Annual Review of Fluid Mechanics*, Vol. 21, pp. 137-166 1989.

[4] L. M. Mack. Boundary layer linear stability theory. In *AGARD report, No. 709*, pages 3–1 to 3–81, 1984.

[5] Y.Ma and X.Zhong. Receptivity of a supersonic boundary layer over a flat plate. Part 2:Receptivity to Freestream Sound. *Journal of Fluid Mechanics*, vol.488, pp.79-121, 2003.

[6] Y. Ma and X. Zhong. Receptivity to Freestream Disturbances of Mach 4.5 Flow over A Flat Plate. *AIAA Paper 2002-0140*, January 2002.

[7] Y. Ma and X. Zhong. Receptivity to Freestream Disturbances of Mach 8 Flow over a Sharp Wedge. *AIAA paper 2003-0788*, 2003.

[8] W. Eibler and H. Bestek. Spatial Numerical Simulations of Linear and Weakly Nonlinear Instabilities in Supersonic Boundary Layers. *Theoretical and Computational Fluid Dynamics*, 8:219–235, 1996.

[9] L. M. Mack. Linear Stability Theory and the Problem of Supersonic Boundary-Layer Transition. *AIAA Journal*, Vol. 13, No. 3, pp. 278-289, 1975.

[10] Xiaolin Zhong. High-Order Finite-Difference Schemes for Numerical Simulation of Hypersonic Boundary-Layer Transition. *Journal of Computational Physics*, Vol. 144, pp. 662-709, 1998.

[11] X.Zhong and T.Lee. Nonequilibrium real-gas effects on disturbance/bow shock interaction in hypersonic flow past a cylinder. *AIAA paper 96-1856*, January 1996.

[12] M. R. Malik, R. S. Lin, and R. Sengupta. Computation of Hypersonic Boundary-Layer Response to External Disturbances. *AIAA Paper 99-0411*, January 1999.

[13] M. R. Malik. Stability theory for chemically reacting flows. In D. Arnal and R. Michel, editor, *Laminar-Turbulent Transition, IUTAM Symp., Toulouse, Springer-Verlag*, 1990.

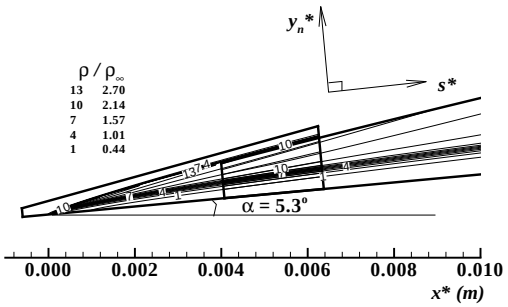

Figure 1: Contours of density near the leading edge for steady base flow(Y.Ma and X.Zhong[7]).

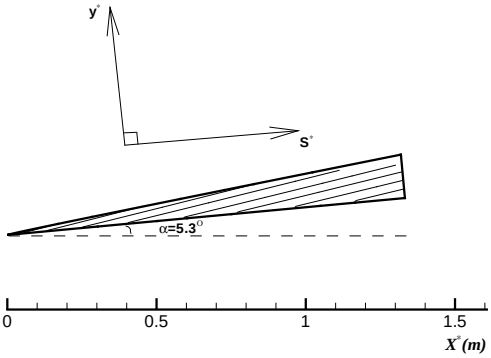

Figure 2: Contours of pressure for steady base flow($Ma_\infty = 8.0$).

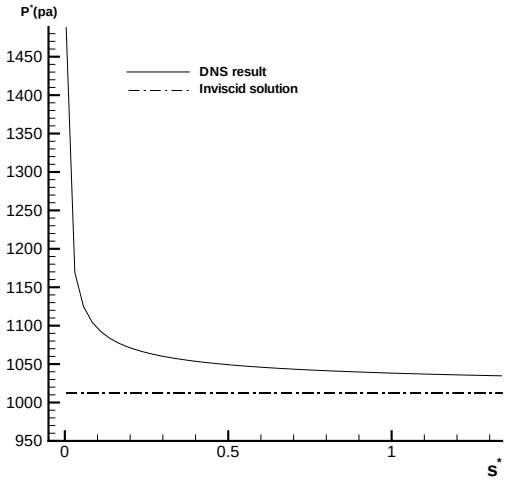

Figure 3: Distributions of pressure along the wall surface for steady base flow over the wedge.

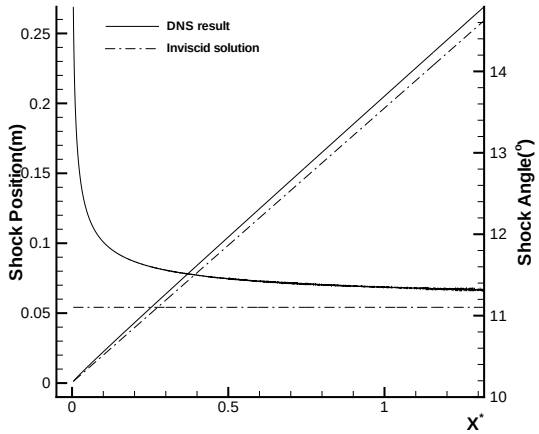

Figure 4: Shock position and shock angle for steady base flow over the wedge.

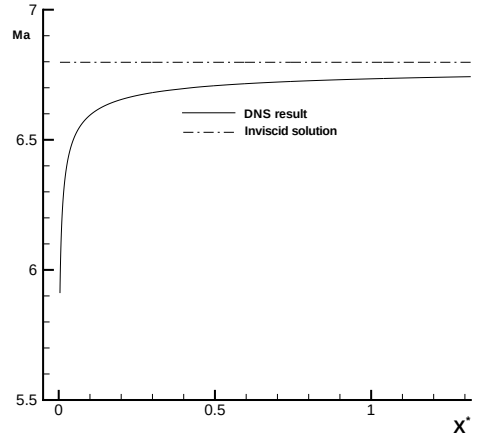

Figure 5: Distribution of the Mach number behind the shock for steady base flow over the wedge.

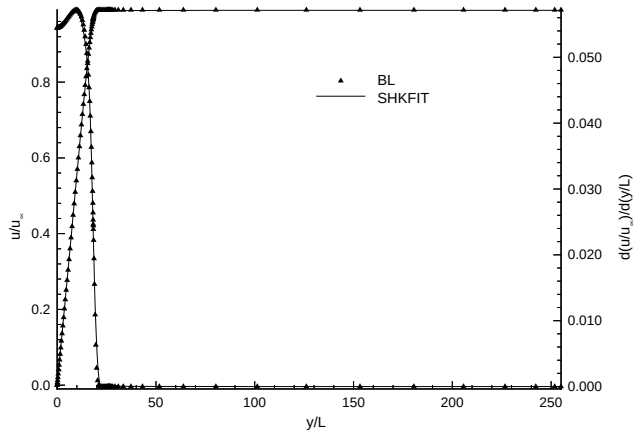

Figure 6: Comparisons of streamwise velocity and its first-order derivative between shock-fitting simulation and boundary layer solution ($s^* = 0.62784m$,$R = 2264.13$)

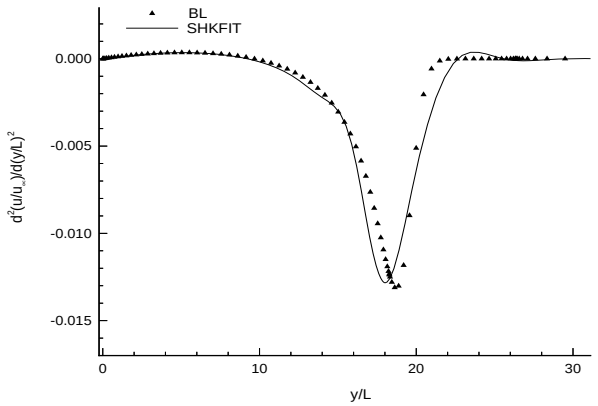

Figure 7: Comparison of the second-order derivative of streamwise velocity between shock-fitting simulation and boundary layer solution ($s^* = 0.62784m$, $R = 2264.13$)

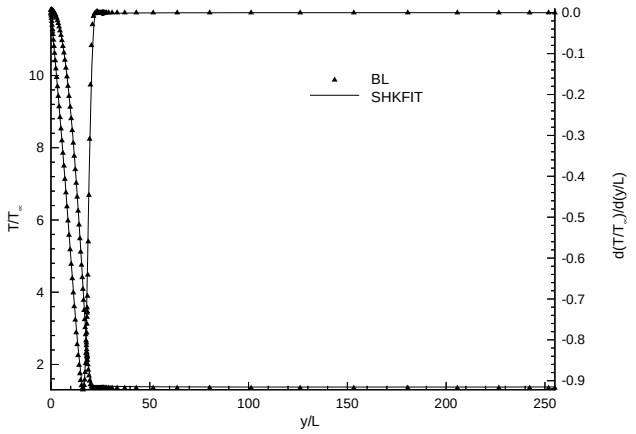

Figure 8: Comparisons of Temperature and its first-order derivative between shock-fitting simulation and boundary layer solution ($s^* = 0.62784m$, $R = 2264.13$)

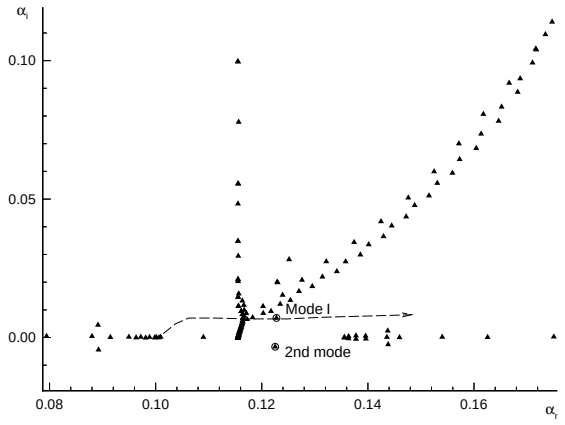

Figure 9: Eigenvalues of boundary layer modes for disturbance with $F = 5.778 \times 10^{-5}$ ($R = 1980.44$).

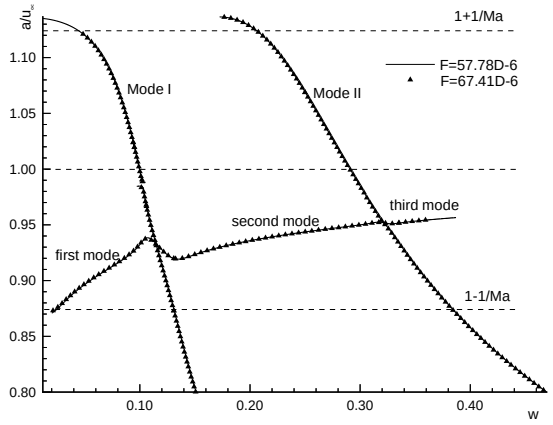

Figure 10: Comparison of non-dimensional phase velocity distributions of normal wave modes inside the boundary layer with different frequencies.

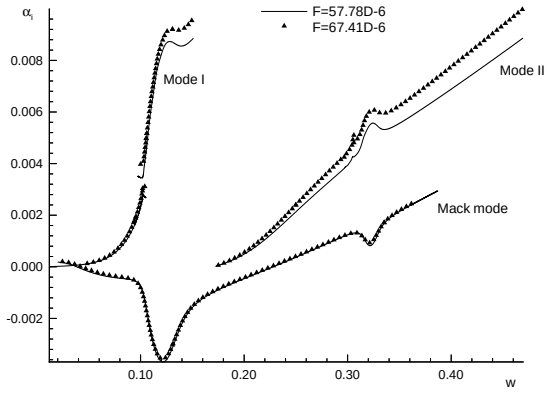

Figure 13: Comparison of the growth rates of boundary layer modes with different frequencies.

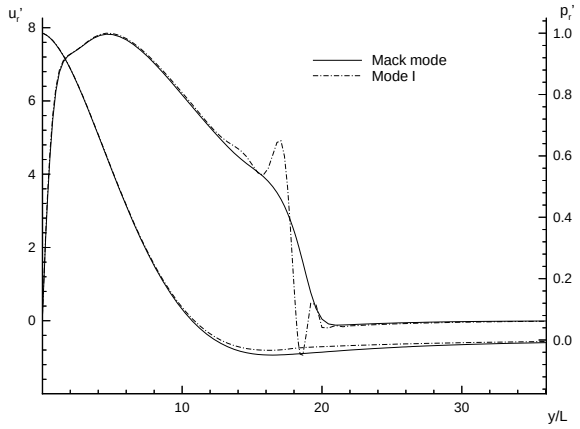

Figure 11: Comparison of eigenfunctions of Mode I and Mack mode at the synchronization point of Mode I and Mack mode.

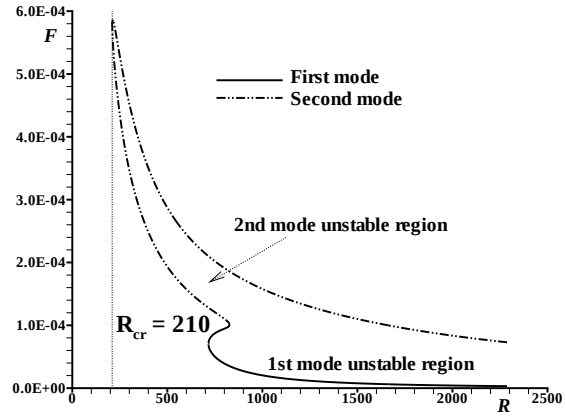

Figure 14: Neutral curve of two-dimensional first and second modes in the hypersonic flow over the wedge (F via R, Y.Ma and X.Zhong[7]).

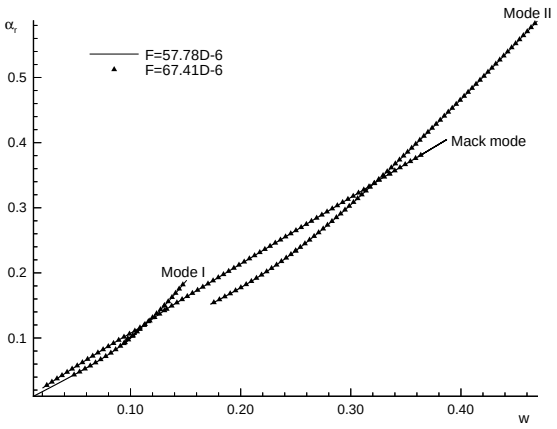

Figure 12: Comparison of the wave numbers of boundary layer modes with different frequencies.

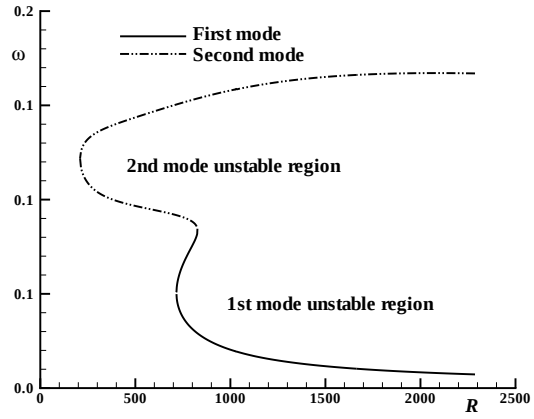

Figure 15: Neutral curve of two-dimensional first and second modes in the hypersonic flow over the wedge (ω via R, Y.Ma and X.Zhong[7]).

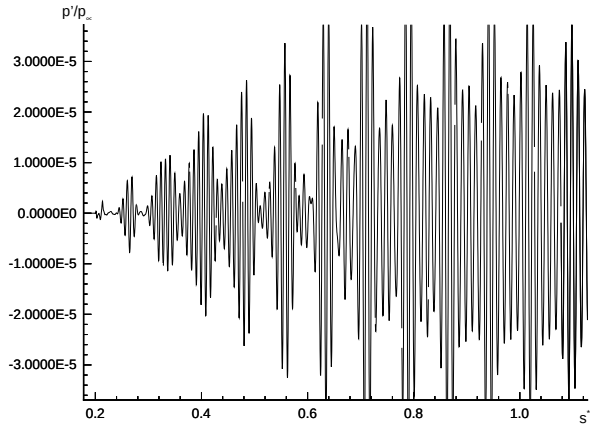

Figure 16: Distribution of instantaneous pressure disturbance along the wedge surface (case 1).

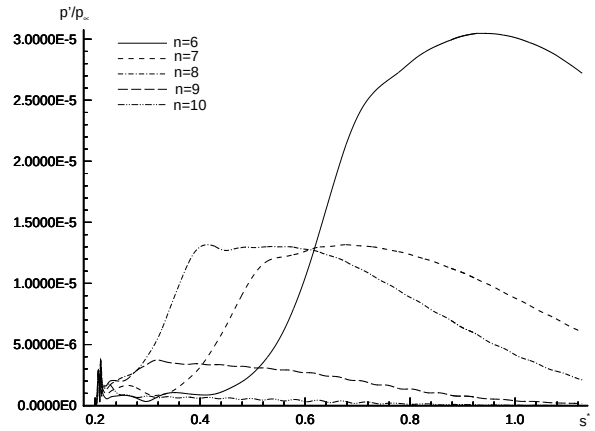

Figure 17: Comparison of pressure perturbations along the wedge surface with different frequencies (case 1).

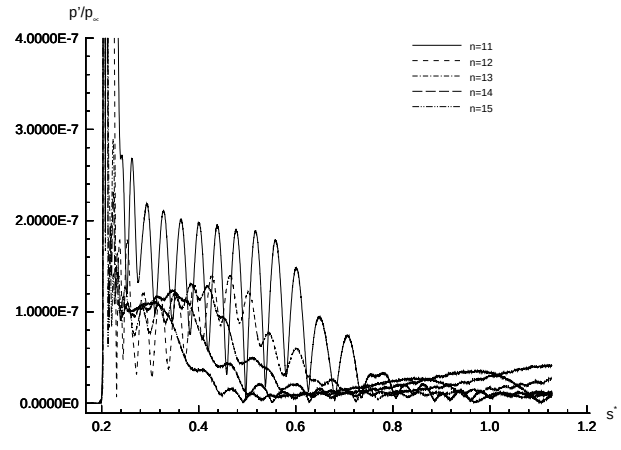

Figure 18: Comparison of pressure perturbations along the wedge surface with different frequencies (case 1).

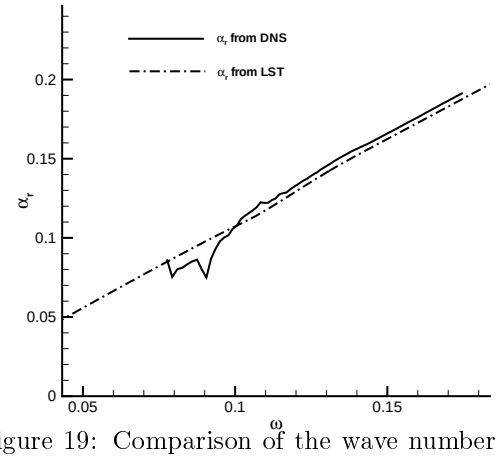

Figure 19: Comparison of the wave number solved by DNS and that of the second mode got by LST ($F = 5.778 \times 10^{-5}$)

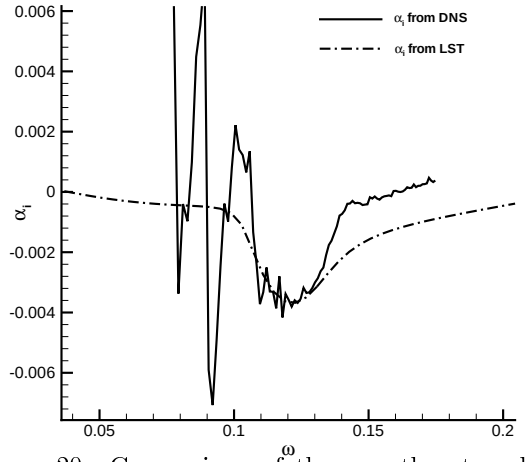

Figure 20: Comparison of the growth rate solved by DNS and that of the second mode got by LST ($F = 5.778 \times 10^{-5}$)

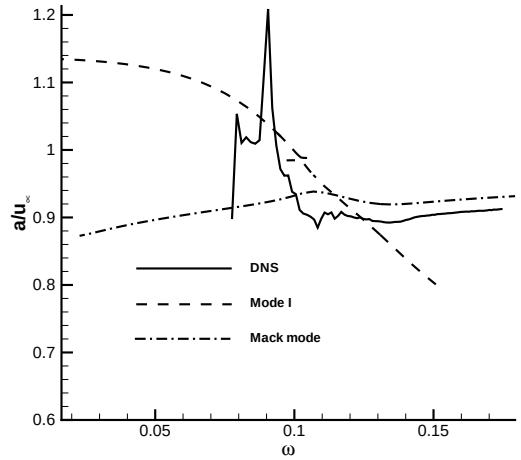

Figure 21: Comparison of the phase velocity solved by DNS and that of the second mode got by LST ($F = 5.778 \times 10^{-5}$)

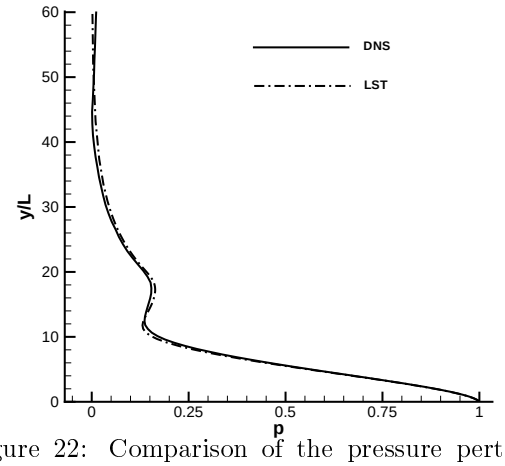

Figure 22: Comparison of the pressure perturbation ($F = 5.778 \times 10^{-5}$) and the second mode eigenfunction at $R = 1975.23$

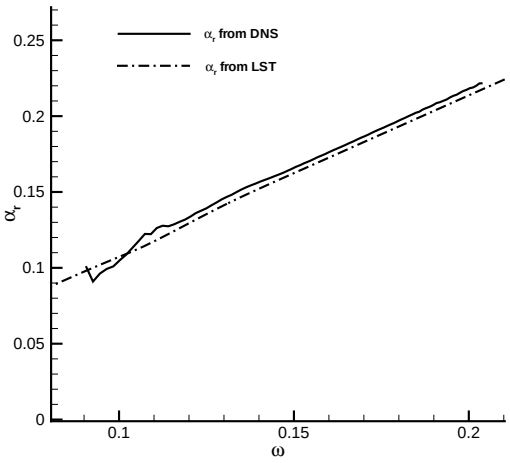

Figure 23: Comparison of the wave numbers solved by DNS and that of the second mode got by LST ($F = 6.741 \times 10^{-5}$).

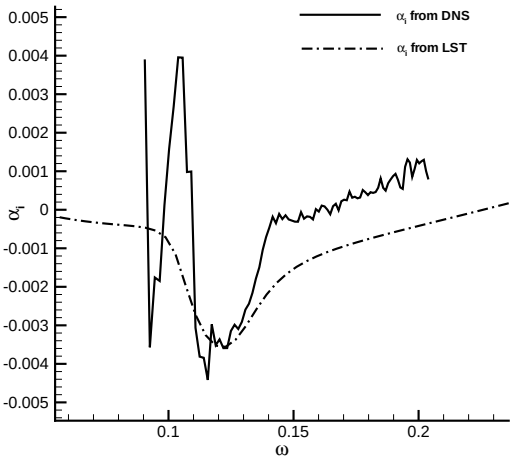

Figure 24: Comparison of the growth rate solved by DNS and that of the second mode got by LST ($F = 6.741 \times 10^{-5}$).

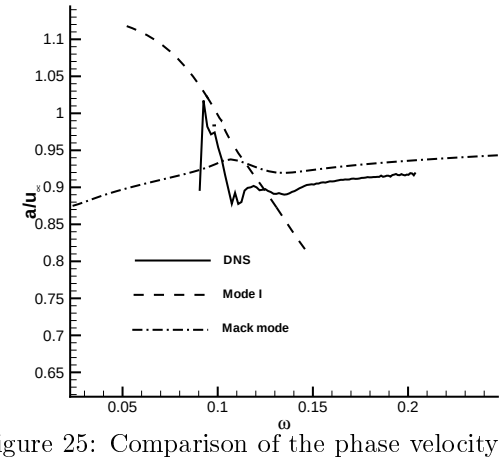

Figure 25: Comparison of the phase velocity solved by DNS and that of the second mode got by LST ($F = 6.741 \times 10^{-5}$).

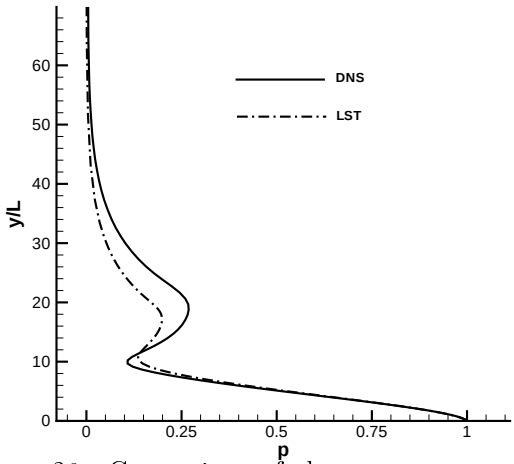

Figure 26: Comparison of the pressure perturbation ($F = 6.741 \times 10^{-5}$) and the second mode eigenfunction at $R = 1756.43$.

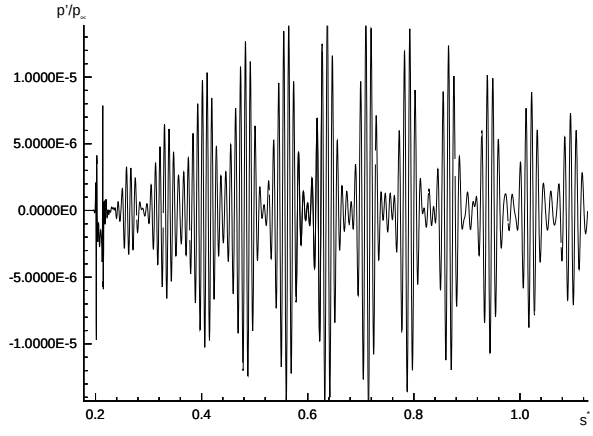

Figure 27: Distribution of instantaneous pressure disturbance along the wedge surface (case 2).

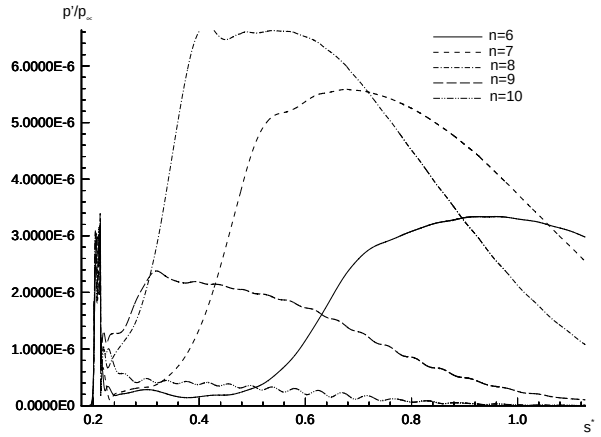

Figure 28: Comparison of pressure perturbations along the wedge surface with different frequencies (case 2).

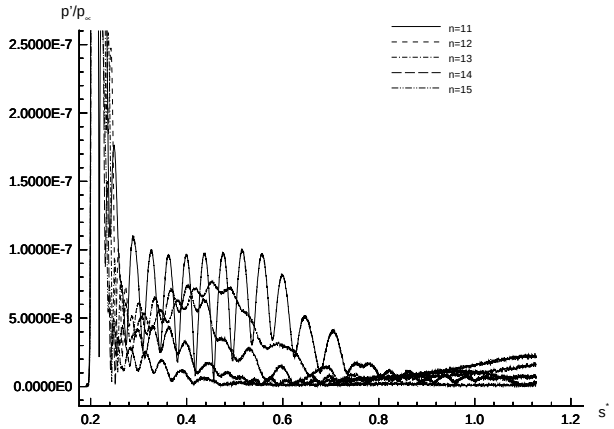

Figure 29: Comparison of pressure perturbations along the wedge surface with different frequencies (case 2).

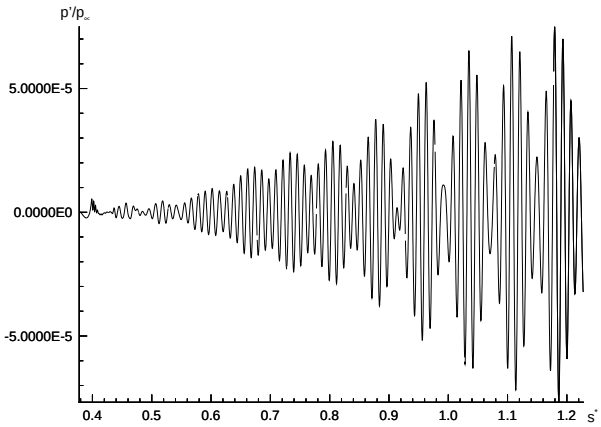

Figure 30: Distribution of instantaneous pressure disturbance along the wedge surface (case 3).

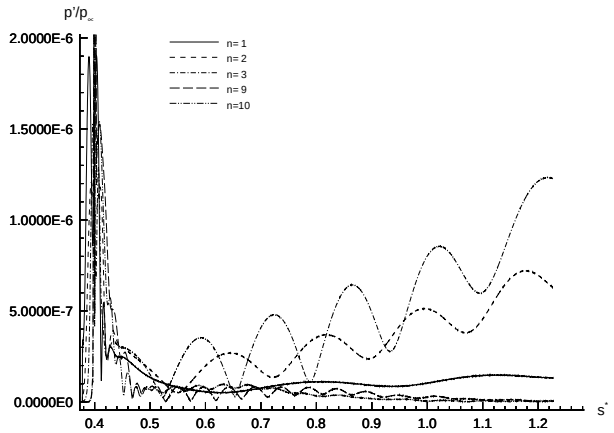

Figure 31: Comparison of pressure perturbations along the wedge surface with different frequencies (case 3).

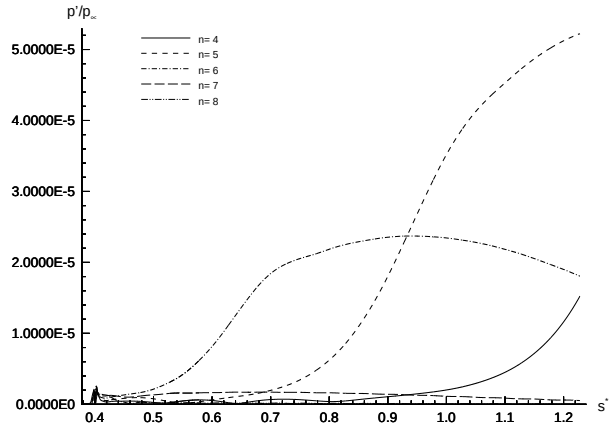

Figure 32: Comparison of pressure perturbations along the wedge surface with different frequencies (case 3).

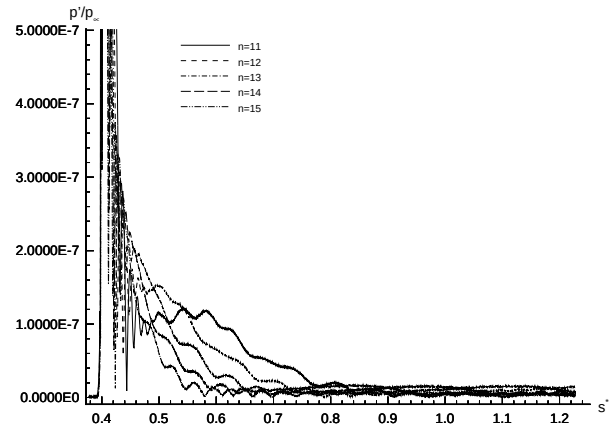

Figure 33: Comparison of pressure perturbations along the wedge surface with different frequencies (case 3).

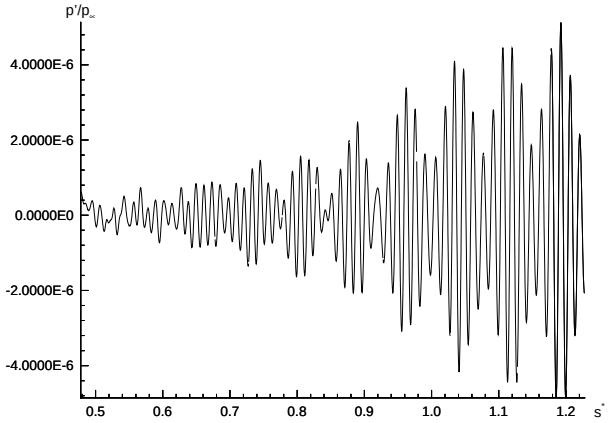

Figure 34: Distribution of instantaneous pressure disturbance along the wedge surface (case 4).

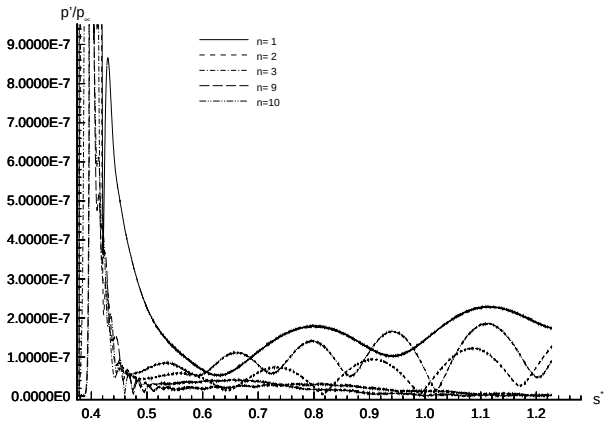

Figure 35: Comparison of pressure perturbations along the wedge surface with different frequencies (case 4).

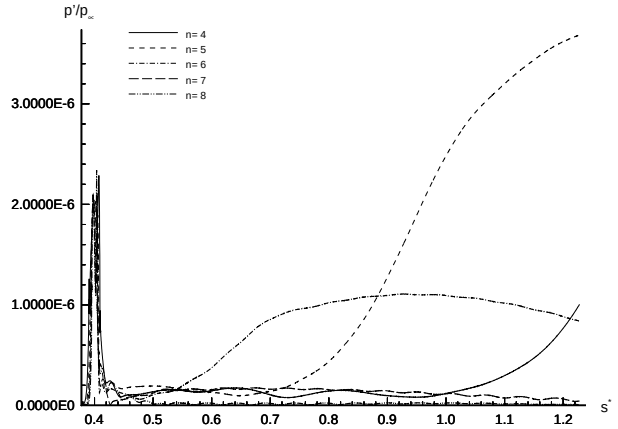

Figure 36: Comparison of pressure perturbations along the wedge surface with different frequencies (case 4).

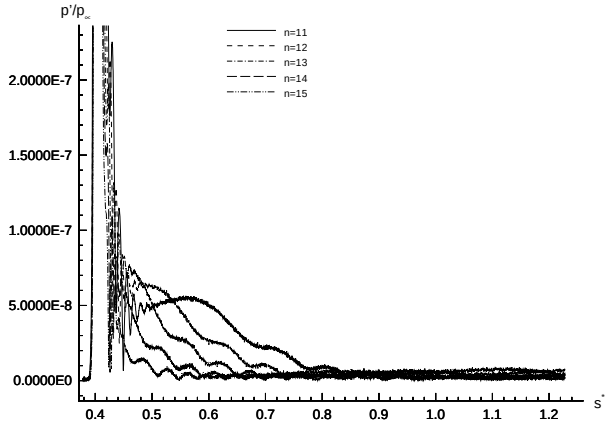

Figure 37: Comparison of pressure perturbations along the wedge surface with different frequencies (case 4).